Multi-eigenmode control for high material contrast in bimodal and higher harmonic atomic force microscopy

Multi-eigenmode control for high material contrast in bimodal and higher harmonic atomic force microscopy

Andreas Schuh[1,2]**, Iman Soltani Bozchalooi**[1]**, Ivo W Rangelow**[2] **and Kamal Youcef-Toumi**[1]

[1] Massachusetts Institute of Technology, Department of Mechanical Engineering, 77 Massachusetts Avenue, Cambridge, MA 02139, USA
[2] Ilmenau University of Technology, Faculty of Electrical Engineering and Information Technology, Dept. of Microelectronic and Nanoelectronic Systems, Gustav-Kirchhoff-Str. 1, 98684 Ilmenau, Germany

E-mail: aschuh@mit.edu

CrossMark

Abstract

High speed imaging and mapping of nanomechanical properties in atomic force microscopy (AFM) allows the observation and characterization of dynamic sample processes. Recent developments involve several cantilever frequencies in a multifrequency approach. One method actuates the first eigenmode for topography imaging and records the excited higher harmonics to map nanomechanical properties of the sample. To enhance the higher frequencies' response two or more eigenmodes are actuated simultaneously, where the higher eigenmode(s) are used to quantify the nanomechanics. In this paper, we combine each imaging methodology with a novel control approach. It modifies the Q factor and resonance frequency of each eigenmode independently to enhance the force sensitivity and imaging bandwidth. It allows us to satisfy the different requirements for the first and higher eigenmode. The presented compensator is compatible with existing AFMs and can be simply attached with minimal modifications. Different samples are used to demonstrate the improvement in nanomechanical contrast mapping and imaging speed of tapping mode AFM in air. The experiments indicate most enhanced nanomechanical contrast with low Q factors of the first and high Q factors of the higher eigenmode. In this scenario, the cantilever topography imaging rate can also be easily improved by a factor of 10.

Keywords: atomic force microscopy, enhanced material contrast mapping, multi-eigenmode control, metrology

(Some figures may appear in colour only in the online journal)

1. Introduction

After its invention in 1986 by Binnig *et al* [1] the atomic force microscope (AFM) has evolved into a versatile tool in nanotechnology. Dynamic modes have been introduced to minimize the potentially damaging forces of the contact mode [2]. Technical advances and new methods allow imaging of topography and other surface characteristics in real-time. In addition, the AFM has been used to map nanomechanical properties. Recently discovered multifrequency techniques use several cantilever frequencies to concurrently obtain topography and material properties.

Both imaging rate and force sensitivity are important factors in the AFM and typically require a trade-off. The overall imaging rate is limited by the scanner, electronics, amplifiers, control feedback loop and the cantilever probe [3–5]. In the intermittent mode, the imaging bandwidth of the cantilever itself can be expressed in terms of an effective Q factor and resonance frequency. Here, low Q factors or high resonance frequencies increase the potential imaging rate

[6, 7]. In contrast, high Q factors are more sensitive to surface forces that allow gentle topography imaging. It also increases the sensitivity of the phase information that is correlated to dissipative tip-sample interactions. Phase imaging has been extensively used for nanomechanical property mapping in the first eigenmode [8–10]. Using higher cantilever eigenmodes can increase both the imaging rate and material sensitivity [11–13].

Modified cantilever dynamics are achieved by control means [7] or appropriate structural probe design. Cantilevers are often manufactured from materials that have very low internal damping and can reach Q factors of up to 500 at ambient pressure. Electronic active resonant control is an approach where the damping of the cantilever is modified by control means in a feedback fashion [14–17]. Q control for a decrease or increase of Q factors can easily be incorporated into existing systems. In particular an electronically based increase of Q factors remains controversial. Ashby [18] shows that using small amplitudes rather than active Q control can be more beneficial. In contrast, a cantilever topology modification through the fabrication process is expensive, time consuming and subject to parameter spread. The modification can include an increased thickness, decreased length or different materials that influence the resonance frequency or intrinsic damping [19, 20].

Recent imaging methods involve two or more cantilever frequencies in a multi-frequency approach [21]. In one method, the first eigenmode is used for topography imaging and the material dependent excitations of higher harmonics are mapped. The higher frequencies appear due the tip periodically and intermittently touching the sample surface [22–26]. Based on the periodicity of the tip-sample force, it can be expanded into a Fourier series [27, 28]. The distribution of the harmonic magnitudes depends on the tip-sample contact time of each cantilever vibration cycle. Mapped with the cantilever transfer function, the response is more or less attenuated depending on the vicinity of nearby eigenmodes. In order to enhance the signal-to-noise ratio (SNR) of higher frequencies, another method uses several concurrently actuated eigenmodes. The first eigenmode maps the topography and the higher eigenmodes are used to map the nanomechanical properties [29–33]. The amplitude and phase of the of the higher eigenmodes can be used to e.g. quantify the sample's Young's modulus. In bimodal actuation (first and second actuated eigenmode), the phase shift of the second eigenmode is one order of magnitude more sensitive to compositional variations than the first one [34]. In both methods, a reference material with known properties is often measured and compared with the sample under investigation to gain quantitative information.

Independently controlling the cantilever eigenmodes in a multifrequency approach can satisfy the requirements of high speed and high sensitivity. Very few attempts have been previously reported to incorporate such a control scheme. However, these have not addressed the multifrequency imaging aspects, in particular toward material contrasts. Such work includes topography imaging with the Q controlled first eigenmode and the suppression of undesired excitations of the second eigenmode. This is done by using a demodulating/modulating based compensator [35]. Ruppert *et al* have introduced an H_∞ approach to suppress undesired excitations of the first eigenmode while performing topography imaging with the second eigenmode [36].

In this work, a novel method combining multi-eigenmode control with multifrequency AFM is demonstrated. In contrast to a simple phase-shift/gain based Q controller the presented compensator automatically separates the different eigenmodes of a single cantilever sensor signal. This enables the independent control of Q factor and resonance frequency in the individual eigenmodes rather than applying the same control action on all eigenmodes. It opens up the possibility to set optimal imaging conditions for topography and material contrast mapping, such as measuring sample stiffness. The bimodal compensator is implemented in a modified AFM setup with an additional lock-in amplifier to capture the higher frequencies. It also utilizes active cantilevers with integrated thermal bimorph actuation and piezo-resistive sensors. The approach is experimentally evaluated. Best results are achieved with low and high Q factors in the first and second eigenmode, respectively.

The presented paper is organized as follows. In section 2, a multi-eigenmode model for the active cantilever is derived and the compensator design is presented in section 3. In section 4, the compensator's discrete implementation into a digital platform is outlined and experimentally validated in the frequency domain. Section 5 presents the application of the compensator toward increased imaging rates and material contrast, this in both introduced multifrequency methods. A conclusion is given in section 6.

2. Multi-eigenmode cantilever model

In this section, an estimated multi-eigenmode model of the cantilever dynamics is obtained. It is derived from measurements, where the output of the model represents the tip displacement upon a harmonic input signal. Modal superposition is valid for small amplitudes and, hence, a linear system can be formed. Previous state-space modeling approaches can be found in [17, 37, 38].

The assumed modal superposition of the active cantilever is confirmed in an experiment. Here, the cantilever is actuated in the first three transverse eigenmodes. This is done in different combinations of added harmonic signals at the respective frequencies. The dc and ac voltages of all actuation signals are 387 and 150 mV peak-to-peak, respectively. The tip amplitudes are measured with a SIOS GmbH, Germany, interferometer (nano vibration analyzer). Table 1 summarizes the result, where the individual components remain nearly constant. A small effect can be seen on an eigenmode, when a lower one is actuated simultaneously. As expected, the total tip displacement amplitude is different for each eigenmode.

The cantilever can be modeled in the form

$$\dot{\mathbf{q}}(t) = \mathbf{A}\mathbf{q}(t) + \mathbf{B}u(t) + w(t), \qquad (1)$$

$$y(t) = \mathbf{C}\mathbf{q}(t) + v(t), \qquad (2)$$

Table 1. Tip vibrational amplitudes in the different actuation combinations (eigenmode = EM).

Actuation	Ampl. EM 1	Ampl. EM 2	Ampl. EM 3
EM 1	244.8 nm	0 nm	0 nm
EM 2	0 nm	84.5 nm	0 nm
EM 3	0 nm	0 nm	13.5 nm
EM 1+2	244.9 nm	84.8 nm	0 nm
EM 1+3	244.8 nm	0 nm	13.9 nm
EM 2+3	0 nm	84.5 nm	13.8 nm
EM 1+2+3	244.8 nm	84.8 nm	13.9 nm

where $\mathbf{A}$ is the state transition matrix, $\mathbf{B}$ the state input vector and $\mathbf{C}$ the state measurement vector, where all have constant coefficients in the linear model. $w(t)$ and $v(t)$ represent the process and measurement noise, respectively. Here, equation (1) describes the dynamic behavior of the cantilever. equation (2) gives an expression for the sensor measurements $y(t)$ in terms of the variables $\mathbf{q}(t)$ and measurement noise $v(t)$.

The model of the cantilever is estimated in the frequency domain through a system identification using the prediction error method [39]. All signal components involved in the future closed feedback loop need to be included to acquire a proper transfer function. The procedure can be carried out automatically. This is necessary every time the cantilever itself or its environment is changed.

The estimated matrices can be expressed as

$$\bar{\mathbf{A}} = \begin{bmatrix} \bar{\mathbf{A}}_1 & \mathbf{0} & \cdots \\ \mathbf{0} & \bar{\mathbf{A}}_2 & \\ \vdots & & \ddots \end{bmatrix}, \bar{\mathbf{B}} = \begin{bmatrix} \bar{\mathbf{B}}_1 \\ \bar{\mathbf{B}}_2 \\ \vdots \end{bmatrix}, \bar{\mathbf{C}} = \begin{bmatrix} \bar{\mathbf{C}}_1 & \bar{\mathbf{C}}_2 & \cdots \end{bmatrix}, \quad (3)$$

where $\bar{\mathbf{A}}$, $\bar{\mathbf{B}}$ and $\bar{\mathbf{C}}$ are the experimentally determined matrices/vectors of $\mathbf{A}$, $\mathbf{B}$ and $\mathbf{C}$, respectively. Each of them contains sub-matrices/vectors representing a separate modeled eigenmode, indicated by the indexes. The block diagonal modal representation is suitable for the hardware implementation discussed in section 4. To reduce computational effort, the model is reduced in its order prior to the compensator design. The Q_i factor and natural frequency $\omega_{n,i}$ of each eigenmode i can be found through the eigenvalues of the estimated model.

In the frequency domain, figure 1 presents a measured cantilever response (black curve) and its estimated models (red, green curves). The exemplary applied multi-eigenmode control (blue curve) is discussed in the frame of the compensator design in section 3. The input is the cantilever actuation signal and the output is the amplified sensor bridge voltage. Figures 1(a) and (b) are the magnitude and phase, respectively. The eighth order model (red curve) correctly predicts the cantilever sensor signal. The reduced discrete forth order model (green curve) shows a difference at off-resonance locations. As its scale is logarithmic the error is very small. Figure 1(c) presents a zoom into the resonance locations of figures 1(a) and (b), indicated by gray dashed ellipses. The corresponding datasets are referred to by numbers. It proofs that the areas of interest are modeled correctly.

3. Multi-eigenmode control approach

In the following, the full state feedback control approach based on a prediction estimator is introduced. The estimator is derived first, giving access to the unmeasured states of the cantilever. This is necessary, as the cantilever sensor only supplies displacement proportional signals. The controller is designed thereafter, based on the cantilever's actual and desired dynamics. The combination of estimator and controller forms the compensator [40]. Note that the compensator incorporates a cantilever model describing its dynamics. Hence, it acts on the raw sensor signal prior any demodulation, such as by lock-in amplifiers.

3.1. Estimator design

A full state estimator is chosen to estimate both the unmeasured velocity and measured displacement of the tip vibrations. Including the latter one improves noise in the system. The tip velocity is required as it directly affects the Q_i of the eigenmodes. Specifically, a steady state Kalman filter is used. As the sampling rate is attempted to be maximized, the relationship of computation to sampling time is close to unity. Hence, the estimator is set up in the predictive form with its discrete time representation

$$\hat{\mathbf{q}}_{\mathbf{k+1}} = \bar{\mathbf{A}}\hat{\mathbf{q}}_{\mathbf{k}} + \bar{\mathbf{B}}u_k + \mathbf{L}\left(y_k - \hat{y}_k\right). \quad (4)$$

The states $\hat{\mathbf{q}}_{\mathbf{k}}$ are estimates of the states $\mathbf{q}_{\mathbf{k}}$. $\hat{y}_k = \bar{\mathbf{C}}\hat{\mathbf{q}}_k$ and $y_k = \mathbf{C}\mathbf{q}_k + v_k$ are the estimated and measured cantilever displacement signal, respectively. y_k with its noise v_k forms one of the two inputs to the estimator and is multiplied by the estimator gain $\mathbf{L}$. Thus, higher gains result in faster poles that improve convergence, but also amplify the noise effects. As the estimator also acts as a filter the overall noise of the feedback signal, dependent on $\mathbf{L}$, is lower than with a regular phase-shift/gain Q controller.

3.2. Controller design

The dynamics of each modeled eigenmode can be modified arbitrarily and independently. Based on the model of equation (3), it offers the possibility to modify Q_i and/or the resonance frequency $\omega_{r,i}$ of the ith eigenmode.

In combination with the reference signal r from the AFM, a controller $\mathbf{K}$ forms the modified cantilever input u_k as

$$u_k = -\mathbf{K}\mathbf{q}_{\mathbf{k}} + Nr_k. \quad (5)$$

N can be used to eliminate the steady state error introduced by the state feedback. The computation of the controller $\mathbf{K}$ is based on the cantilever dynamics and desired pole locations. The dynamics of each eigenmode are modified either toward a desired Q factor $Q_{\text{des},i}$, a desired resonance frequency $\omega_{r_{\text{des}},i}$ or a combination of both. The poles are defined in the continuous time (*s*-domain) that are converted into the discrete time domain (*z*-domain) afterwards.

In the following, a strategy is outlined to determine the desired closed loop pole locations. A desired conjugate complex $p_{i_{1,2}}$ pole pair for the control of each Q_i and $\omega_{r,i}$ can
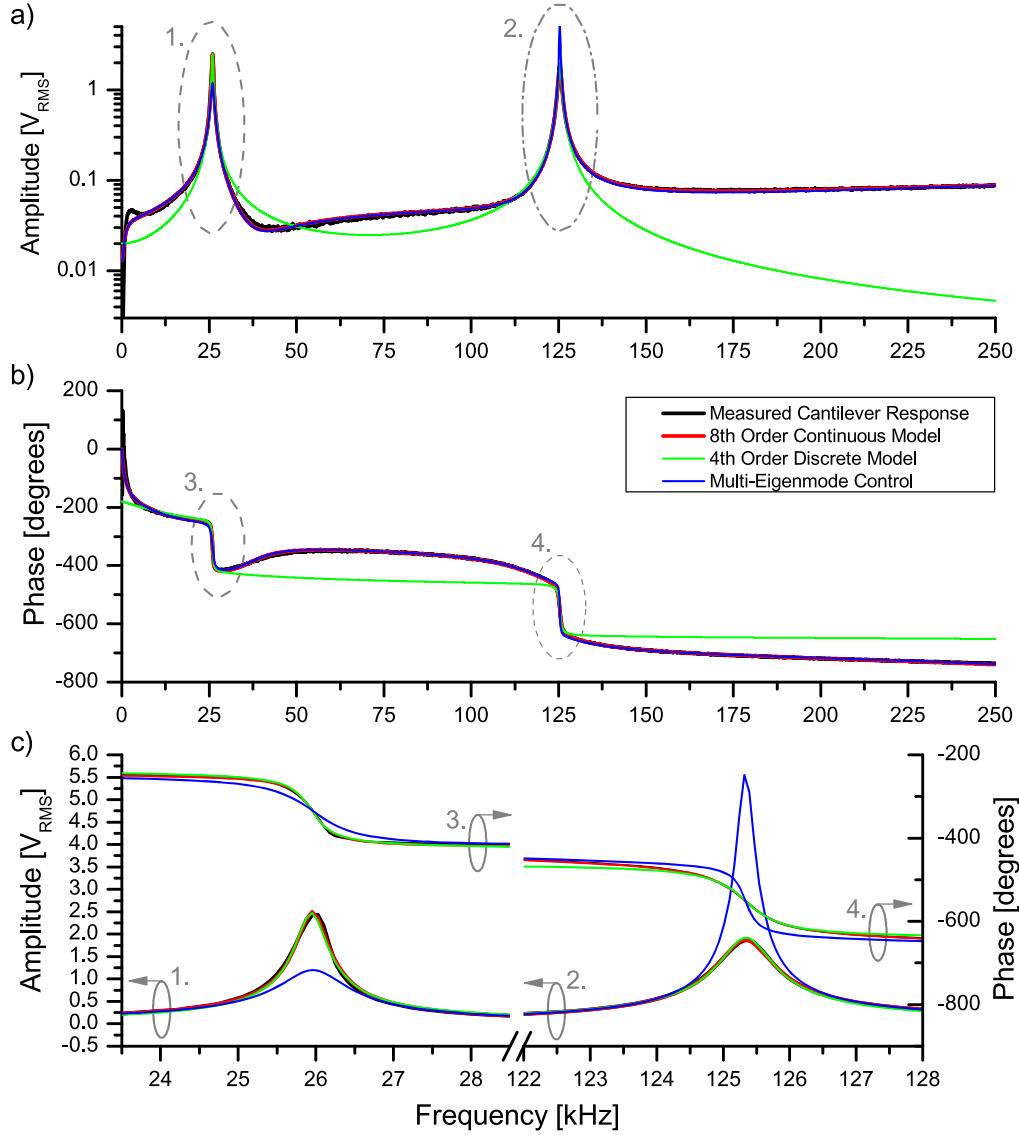
Figure 1. Comparison of magnitude (a) and phase (b) of the cantilever sensor signal (black curve) and its model estimates (red, green curves). A simulation decreasing Q_1 and increasing Q_2 is indicated by the blue curve. Diagram (c) is a zoom into both resonances for better visibility, whose locations are indicated by numbers and gray ellipses in (a) and (b).

be found by the relationship

$$p_{i_{1,2}} = \frac{\omega_{r,i}}{\sqrt{1 - 1/\left(2Q_{c,i}^2\right)}}\left(-\frac{1}{2Q_{\text{des},i}} \pm \sqrt{\frac{1}{4Q_{\text{des},i}^2} - 1}\right). \quad (6)$$

$Q_{c,i}$ is a design parameter and can be substituted by either Q_i or $Q_{\text{des},i}$. The dynamics can be influenced in the following ways, where (A), (B) are for Q control, (C) for frequency control and (D) a combination of both:

(A) by substitution of $Q_{c,i} = Q_i$ and choosing $Q_{\text{des},i}$, each eigenmode can be modified in its Q factor only. Here, $\omega_{r,i}$ naturally changes with varying closed loop $Q_{\text{des},i}$ based on $\omega_{r,i} = \omega_{n,i}\sqrt{1 - 1/(2Q_{\text{des},i}^2)}$. A variation of $Q_{\text{des},i}$ in a sweep fashion causes the pole pairs to form a circular movement in the complex plane (figure 2(a)). It starts close to the imaginary axis for high $Q_{\text{des},i}$ and

meets the negative real axis in the critically damped case of low $Q_{\text{des},i}$. The increase of $Q_{\text{des},i}$ moves the poles closer to the imaginary axis, potentially leading to instabilities,

(B) by substitution of $Q_{c,i} = Q_{\text{des},i}$ and choosing $Q_{\text{des},i}$, $\omega_{n,i}$ is modified such that $\omega_{r,i}$ is kept constant at $\omega_{n,i}\sqrt{1 - 1/(2Q_i^2)}$. Figure 2(b) indicates the formation of such poles in the complex plane with a sweep of $Q_{\text{des},i}$. Note that in this case Q_i and $\omega_{n,i}$ are both modified,

(C) by substitution of $\omega_{r,i} = \omega_{r_{\text{des}},i}$ and $Q_{c,i} = Q_{\text{des},i} = Q_i$ the resonance frequency is modified. This can be seen in figure 2(c), indicating the formation of such poles in the complex plane with a sweep of $\omega_{r_{\text{des}},i}$. Q_i is kept constant in all cases, visible by the unmodified angle of the pole locations to the origin,
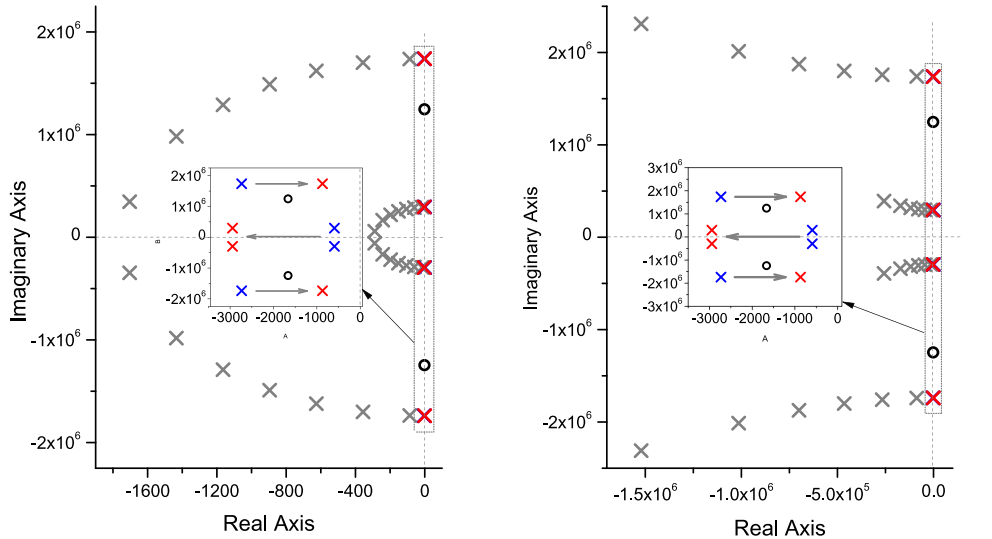
(a) Q Control pole formation keeping $\omega_{n,i}$ constant by substituting $Q_{c,i} = Q_i$.

(b) Q control pole formation keeping $\omega_{r,i}$ constant by substituting $Q_{c,i} = Q_{des,i}$.
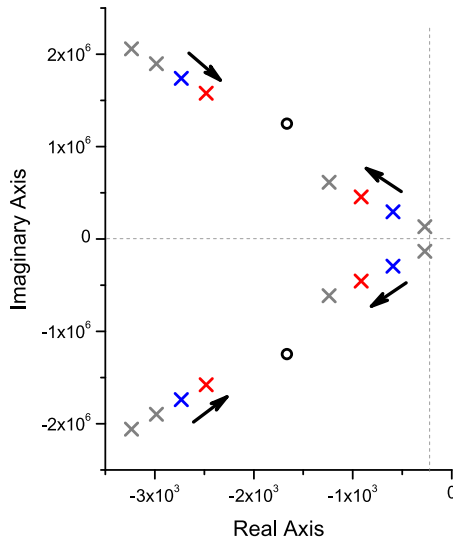
(c) F control pole formation modifying $\omega_{r,i}$ and keeping $Q_{c,i} = Q_i$ constant.

Figure 2. In (a) and (b) either $\omega_{n,i}$ or $\omega_{r,i}$ is kept constant, resulting either in a naturally modified or a forced constant $\omega_{r,i}$ upon Q control. The inlets magnify a case, where, indicated by arrows, Q_1 is decreased and Q_2 increased. The zeros remain unaffected. In (c) $\omega_{r,i}$ of two eigenmodes are modified, where $Q_{c,i} = Q_i$ is kept constant.

(D) by substitution of $\omega_{r,i} = \omega_{r_{des},i}$, $Q_{c,i} = Q_i$ and choosing $Q_{des,i}$ both resonance frequency and Q factor can be modified arbitrarily.

Distinguishing between the two above cases (A) and (B) may result only in small differences in the resonances. This is in particular true for cantilevers in air and vacuum with relatively high Q_i and $Q_{des,i}$. In contrast, the cantilever's damping is much higher in water and the difference more pronounced, giving this strategy a potential application.

On a side note, arbitrarily placed pole pairs are often not practicable. Increasing the Q factors toward very high values is prone to instabilities due to positive feedback of the
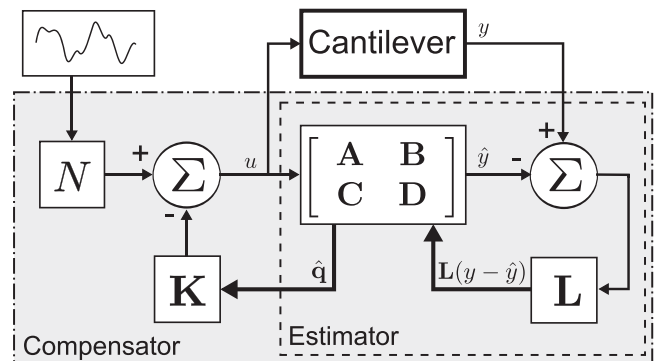

Figure 3. The compensator composed of controller and estimator, connected to the active cantilever and external actuation.
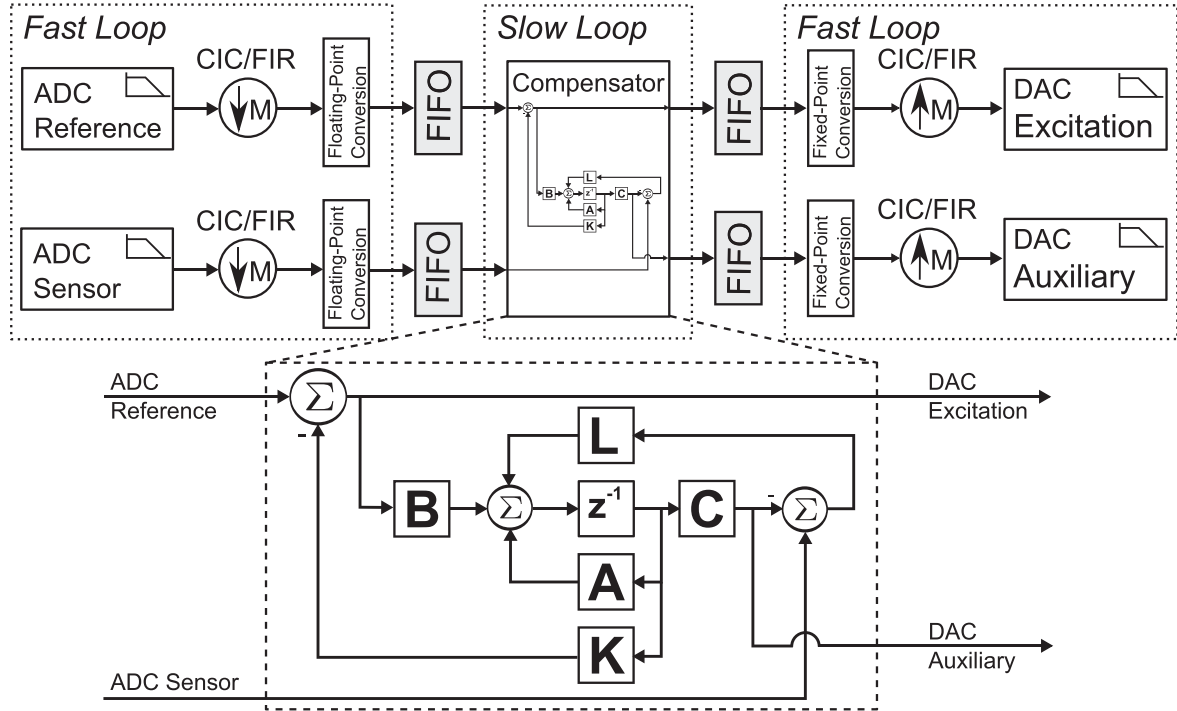
Figure 4. Overview of the digital implementation in the FPGA systems.

compensator. In contrast, very low Q factors can be unfeasible as the resonance curves become flat. The maximum control action is mostly limited by the cantilever's actuator.

3.3. Combined controller, estimator and cantilever

The controller of section 3.2 is combined with the estimator of section 3.1 and the resulting compensator connected to the cantilever. Hence, $\mathbf{q_k}$ of equation (5) is replaced by the state estimates $\hat{\mathbf{q}}_\mathbf{k}$ of equation (4):

$$u_k = -\mathbf{K}\hat{\mathbf{q}}_\mathbf{k} + Nr_k. \tag{7}$$

Combination of controller and estimator results in

$$\hat{\mathbf{q}}_{\mathbf{k+1}} = \left(\bar{\mathbf{A}} - \bar{\mathbf{B}}\mathbf{K} - \mathbf{L}\bar{\mathbf{C}}\right)\hat{\mathbf{q}}_\mathbf{k} + \mathbf{B}Nr_k + \mathbf{L}y_k, \tag{8}$$

which is combined with the cantilever's dynamics to form

$$\begin{bmatrix} \mathbf{q}_{k+1} \\ \hat{\mathbf{q}}_{k+1} \end{bmatrix} = \begin{bmatrix} \mathbf{A} & -\mathbf{B}\mathbf{K} \\ \mathbf{L}\mathbf{C} & \bar{\mathbf{A}} - \bar{\mathbf{B}}\mathbf{K} - \mathbf{L}\bar{\mathbf{C}} \end{bmatrix} \begin{bmatrix} \mathbf{q}_k \\ \hat{\mathbf{q}}_k \end{bmatrix} +$$
$$+ \begin{bmatrix} \mathbf{B}N \\ \bar{\mathbf{B}}N \end{bmatrix} r_k + \begin{bmatrix} \mathbf{B} \\ 0 \end{bmatrix} w_k + \begin{bmatrix} 0 \\ \mathbf{L} \end{bmatrix} v_k, \tag{9}$$

$$\begin{bmatrix} y_k \\ \hat{y}_k \end{bmatrix} = \begin{bmatrix} \mathbf{C} & 0 \\ 0 & \bar{\mathbf{C}} \end{bmatrix} \begin{bmatrix} \mathbf{q}_k \\ \hat{\mathbf{q}}_k \end{bmatrix} + \begin{bmatrix} 1 \\ 0 \end{bmatrix} v_k. \tag{10}$$

The output equation $[y_k\ \hat{y}_k]'$ holds the cantilever sensor and estimated measurement, where the latter one is drastically reduced in noise. Figure 3 is a block diagram presenting the combined compensator and cantilever setup according to equations (9) and (10).

A combined continuous/discrete time simulation performed in the frequency domain is presented by the blue curve in figure 1. In this case, the compensator is designed with the reduced fourth order discrete time domain model, indicated by the green curve in figure 1. The compensator is acting on the more accurate eighth order continuous time model to represent a realistic cantilever behavior. As designed, Q_1 is decreased and Q_2 increased. This example clearly shows that the lower order compensator is able to properly control the first and higher eigenmodes of the cantilever simultaneously.

4. Compensator implementation

The compensator is implemented digitally into two different field programmable gate array (FPGA) platforms with fast analog-to-digital (ADC) and digital-to-analog converters (DAC), using a state machine structure and floating point representation. The first platform is a National Instruments (NI) FlexRIO PXI-7954 R board equipped with a Virtex 5 LX-110 FPGA and programmed with NI LabVIEW FPGA. A Baseband Transceiver 5781 with 100 MHz ADCs/DACs is connected for fast sampling. The second platform is a Trenz Electronic board with a Spartan-3A DSP, placed on a custom hardware board equipped with 100 MHz converters and configured with VHDL.

The logic implementation is comparable on both platforms The Virtex-5 one is shown in figure 4. The clock domains *fast loop* and *slow loop* execute different parts of the code. The communication between the two is realized by first in, first out memories. Decimators/interpolators are implemented either through cascaded integrator–comb or finite impulse response filters for the prevention of aliasing after a
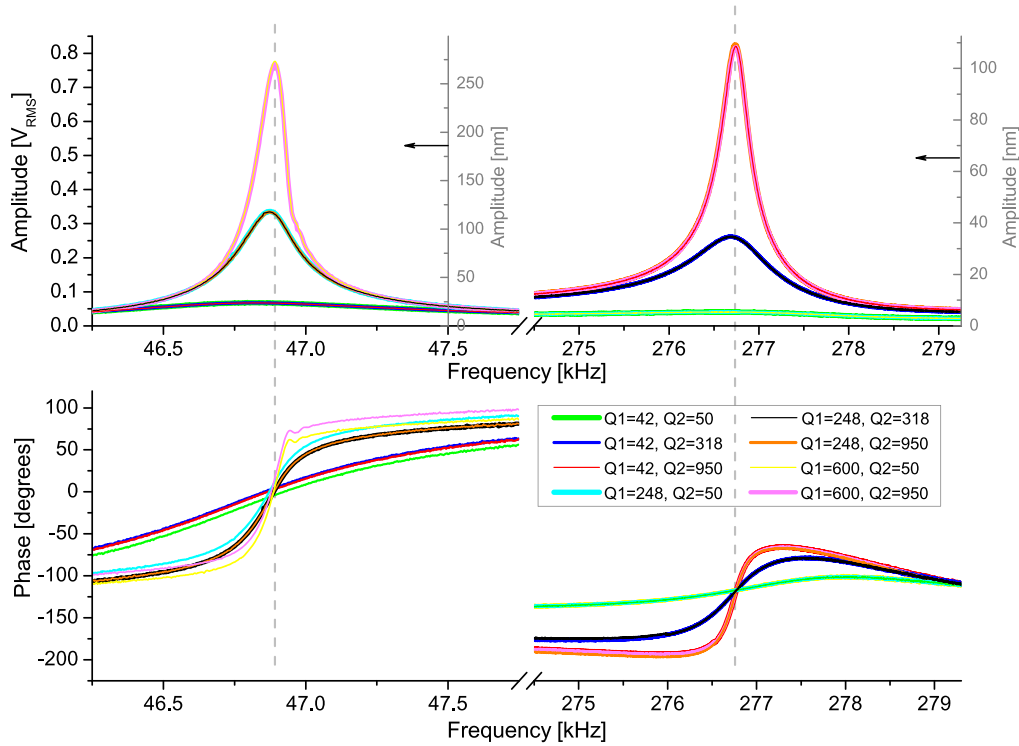
Figure 5. Frequency sweeps of the first two transverse eigenmodes with applied multi-eigenmode Q control. Every curve is colored based on an individual combination of Q_1 and Q_2. The vibrational amplitude of each eigenmode is indicated by the gray ordinates.

sample rate change. The zoomed area indicates the compensator logic that is implemented according to equation (8). The *ADC reference* and *ADC sensor* are the actuation signal from the AFM controller and the cantilever's sensor signal, respectively. The *DAC excitation* and *DAC auxiliary* are the modified cantilever actuation signal and the estimated cantilever sensor signal $\hat{\mathbf{C}}\hat{\mathbf{q}}_{\mathbf{k}}$, respectively.

A state-machine structure consisting of nine states computes the compensator feedback loop. That way, hardware components can be reused and assigned with different tasks each state iteration. This saves potentially valuable space and components inside the FPGA. Also, splitting the computations allows higher clock rates that otherwise introduce long signal paths. Our experience has shown that the depth of such pipelining and achieved clock rate form an optimum trade-off. In that case, the resulting compensator feedback loop rate is maximized. The computations are performed by a total of four multipliers, four adders and one subtractor. The updated actuation signal u_k can be processed as quickly as possible to reduce compensator time delay. After new incoming samples, it is the first computation performed in a time step k. All other compensator loop computations, now needed for time step $k + 1$, can be prepared during the remaining time of k. In addition, the compensator computation in the FPGA can be partly parallelized, mostly applying to matrix operations. In the Virtex-5, an overall compensator feedback loop rate of 5.56 MHz is achieved. In contrast, the rate in the Spartan-3A is 2.77 MHz.

Figure 5 shows various experimental frequency sweeps of the first two transverse eigenmodes with the modified Q_i's
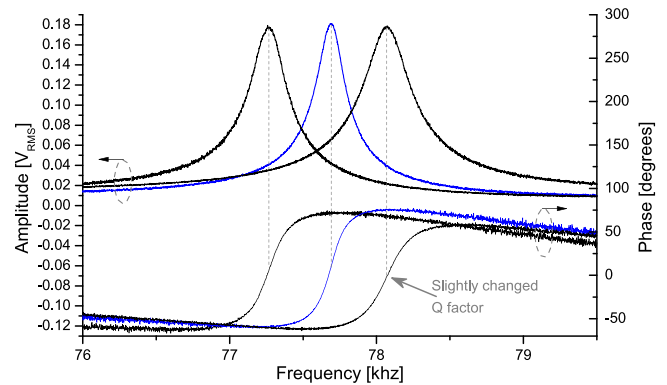

Figure 6. Applied frequency control. The blue curve is a frequency sweep of the cantilever with unmodified $\omega_{r,1}$. The black curves indicate the modified resonances. The arrow indicates an unintentionally reduced Q_i.

as indicated. Each combination of Q_1 and Q_2 is a single sweep including both eigenmodes. Hence, the curves with similar Q_i's in either eigenmode are on top of each other, drawn with varying line thicknesses. This is to indicate the independent tuning capabilities of the two eigenmodes by the compensator. The actuation voltage results in different vibration amplitudes in each eigenmode. The interferometric determined values are indicated by gray ordinates, with arrows pointing toward the respective eigenmode.

A different compensator design is able to modify $\omega_{r,i}$ of the cantilever. Figure 6 indicates the first eigenmode, where the blue curve is the unmodified $\omega_{r,1}$ with its ϕ_1. The black curves are the modified $\omega_{r,1}$'s, with one being higher and one
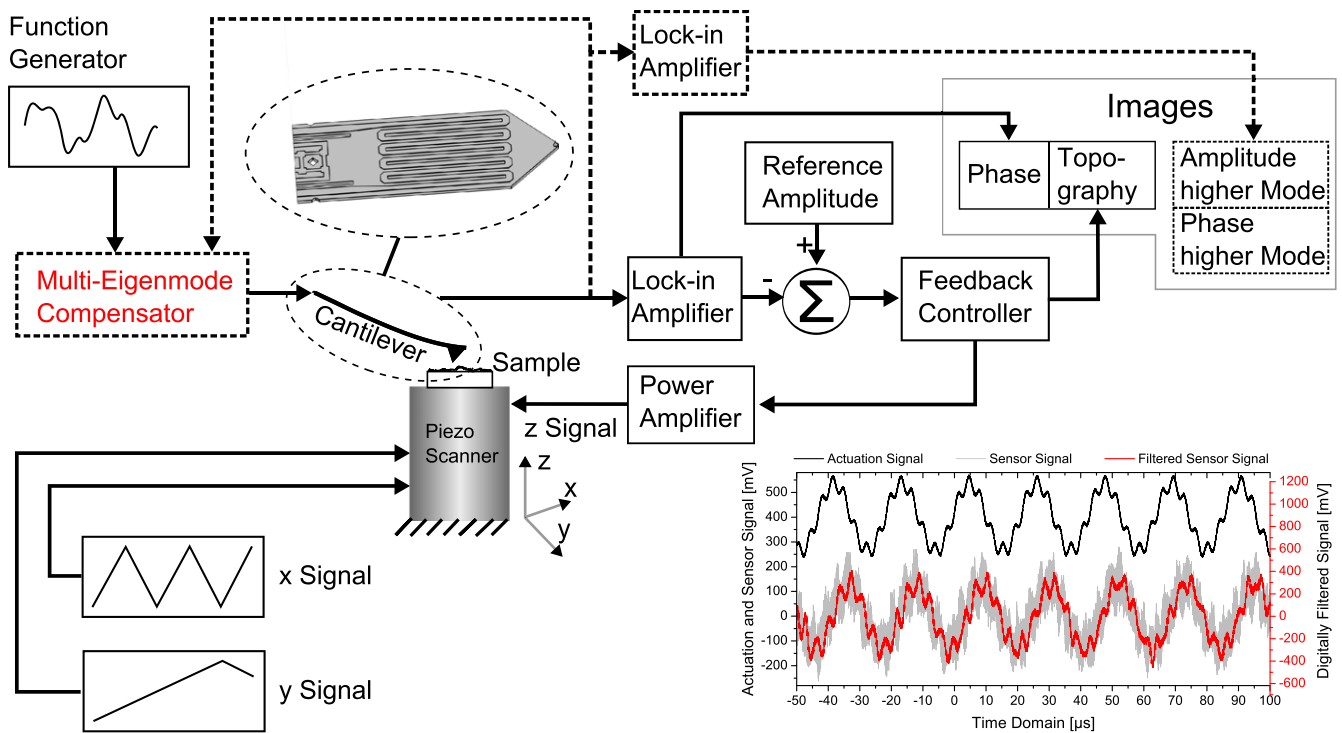
Figure 7. Modified AFM setup for the multi-eigenmode control approach. Dashed lines and boxes indicate the modification of the standard setup. The time domain signals of the diagram show the raw and filtered/amplified bimodal actuation response of the active cantilever.

lower than the unmodified resonance. Although not intended by the design, the resonance corresponding to the increased $\omega_{r,1}$ shows a decreased Q_1. This is indicated by the arrow, and can be seen by the decreased slope of the phase and widened resonance curve.

5. Multifrequency control imaging results and discussion

In this section, the imaging and characterization performance of the multifrequency methods in combination with the multi-eigenmode compensator are investigated.

5.1. Experimental setup

The modified AFM setup shown in figure 7 is utilized in the following experiments. It is a standard setup that is extended by new signal paths, the multi-eigenmode compensator and a second lock-in amplifier, represented by dashed lines and boxes. The compensator acts on the raw sensor signal to modify the cantilever's dynamics. In contrast, the lock-in amplifiers are used to demodulate the signals for data presentation and control of the *z*-piezo. The signals of the second lock-in amplifier are plotted alongside with the topography and phase that correspond to the first eigenmode.

The cantilevers utilized have integrated thermal expansion based bimorph actuation. The displacement proportional piezo-resistive sensors form a Wheatstone bridge configuration for enhanced sensitivity [41, 42]. The time domain signals of the diagram in figure 7 show the bimodal actuation of

the active cantilever with its raw and filtered/amplified response. The cantilever of figure 5 is used throughout this section.

The utilized sample is a Bruker PS-LDPE-12M, a two component polymer blend with different elastic moduli spun on a silicon substrate. The polystyrene (PS) appears as a film on the surface, whereas the polyolefin elastomer (LDPE) forms half-spheres. The PS and LDPE regions have Young's moduli of around 2 and 0.1 GPa, respectively.

5.2. Frequency domain measurement results

The modification of Q_1 and Q_2 considerably enhances the response of nearby harmonics. This can be seen in figure 8. A topographic image of the polymer sample allows us to locate the different materials. One at a time, the tip of the cantilever is brought into an intermittent contact with each polymer. Here, the AFM controls the average distance of the tip to the sample without scanning the surface. Figure 8(a) shows a cantilever's discrete Fourier transform spectrum. Visible are the fundamental resonance at 47 kHz (first harmonic) and its excited higher harmonics. The sixth harmonic is pronounced due to the vicinity of the second eigenmode. Figures 8(b) and (c) are zooms into the sixth harmonics on both hard PS and soft LDPE regions, respectively. Concurrently, Q_1 and Q_2 are modified in different combinations, as indicated by the legend of figure 8(c). The combination of low Q_1 and high Q_2 results in the largest SNR on both polymers.

In bimodal actuation, figure 9 presents two frequency sweeps obtained of the second resonance with $Q_1 = 42$ and $Q_2 = 950$ (first resonance not shown). The black curve is a
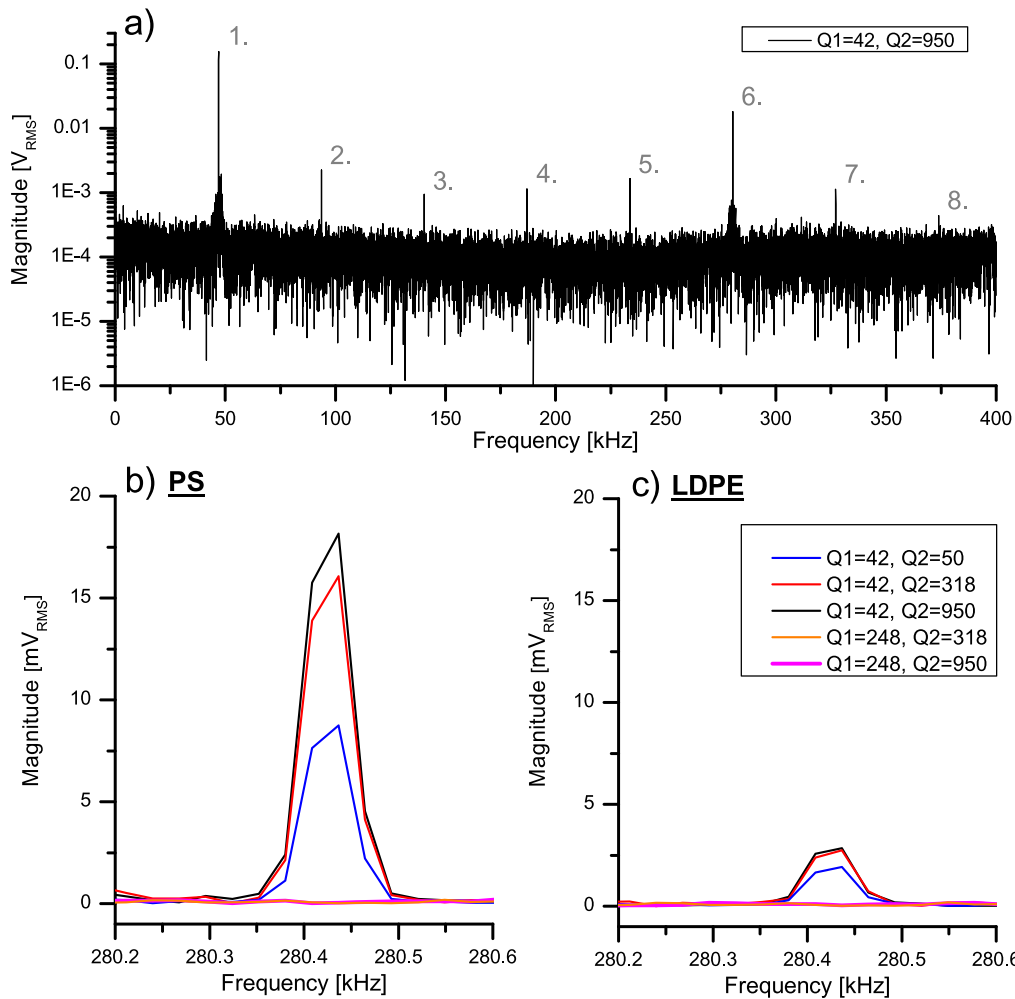
Figure 8. (a) A selected DFT to indicate the fundamental resonance at 47 kHz and its excited harmonics. The *n*th harmonics are indicated by numbers, (b) and (c) are the responses of sixth harmonics while the cantilever intermittently contacts the different polymers. Concurrently, Q_1 and Q_2 are modified. (Legend in (c) applies to both subfigures (b) and (c).)
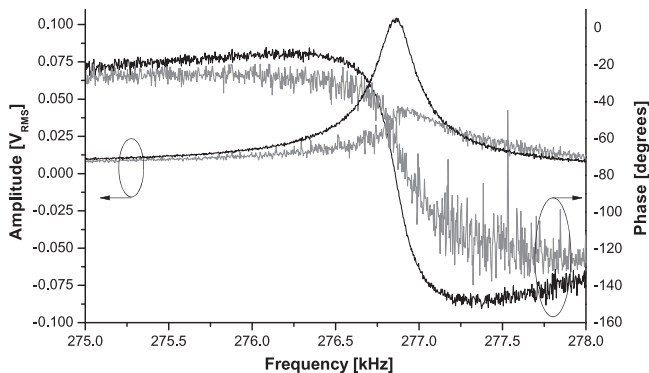

Figure 9. Two frequency sweeps of the cantilever's second resonance; black when the cantilever is in free air and gray when the first resonance's amplitude is used to regulate a specific distance to the sample surface.

sweep of the cantilever in free air. The cantilever is then brought into intermittent contact with a set-point of 45% in the first resonance. The gray curve indicates the influence of the sample surface on the higher cantilever eigenmode's dynamics.

5.3. Imaging results

The imaging performance of the two discussed multi-frequency methods with different combinations of Q_1 and Q_2 is investigated. Figures 10 and 11 contain images obtained concurrently with the first and second eigenmode/sixth harmonic, respectively. All images are within the same scan area of the polymer sample. The different combinations of modified Q factors are indicated as well as the type of response captured. The qualitative comparison indicates enhanced stiffness contrasts such that more details on the sample surface become visible. As stated earlier, the material stiffnesses are known to be 2 and 0.1 GPa. A sample with unknown materials can then be measured quantitatively by a preceding calibration with a sample of known characteristics.

Figures 10 (a) and (b) are the topography and phase (ϕ_1) obtained with the first eigenmode and the natural $Q_1 = 248$ at an actuation frequency of 46.848 kHz. As presented later, in particular a lowered Q_1 factor enables pronounced responses and contrast in the higher eigenmode and harmonic. Hence, figures 10 (c) and (d) are the topography and ϕ_1 obtained with the first eigenmode and a modified $Q_1 = 42$. This also causes
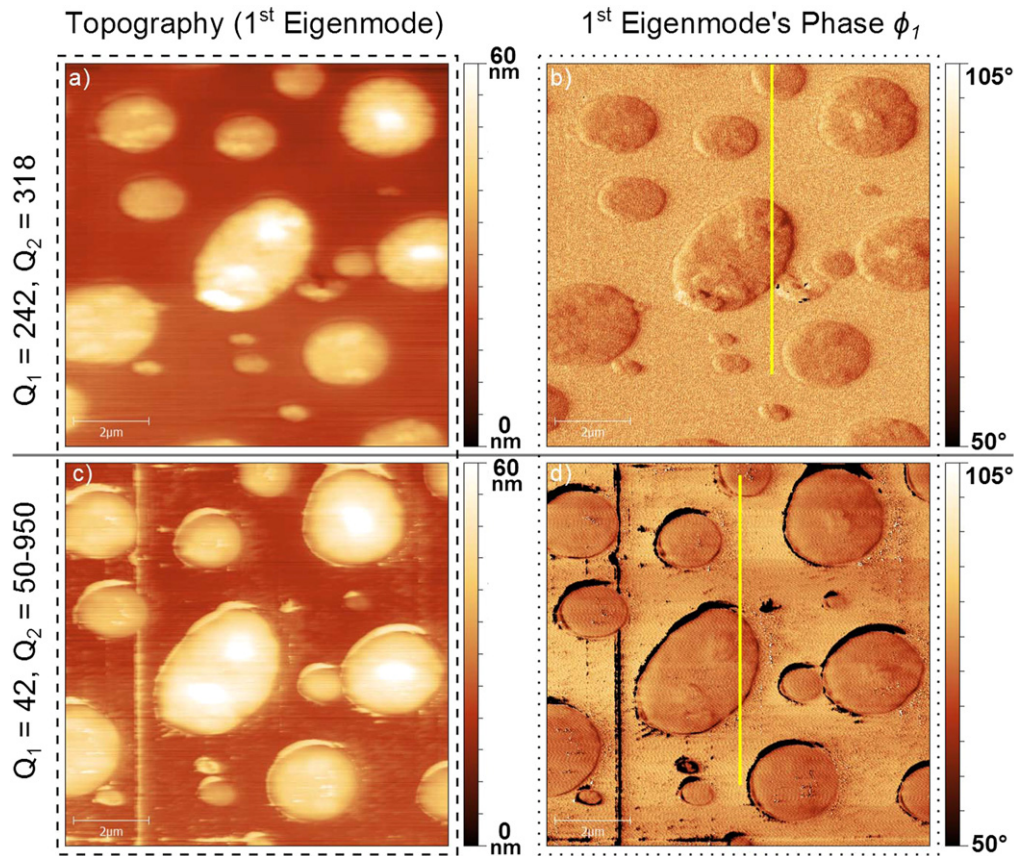
Figure 10. All images are obtained with the first eigenmode. (a) and (b) are the topography and ϕ_1 by using the natural Q factors, (c) and (d) are the topography and ϕ_1 obtained with modified cantilever Q factors, as indicated.

a slightly different resonance and hence actuation frequency of 46.699 kHz, based on the influence of Q_1 on $\omega_{r,1}$. As expected with lower Q factors, the topography in figure 10(c) has a lower resolution, as compared to figure 10(a). The features appear to be squeezed due to the higher forces exerted on the sample. In both cases of figure 10, the free air amplitude at the tip of the cantilever is about 117 nm. This is set by an appropriate actuation signal. The cantilever amplitude set-points are 50%. The scan areas are $(10\ \mu\text{m})^2$ at a scan rate of 2 lines/s.

A set of images with captured responses of the second eigenmode/sixth harmonic with different Q_2 factors is presented in figure 11. The images are simultaneously obtained with the images of figure 10. The column and row labels indicate the type of response measured and used Q factors, respectively. The yellow straight lines are the locations of cross sections presented below in figure 12. In bimodal AFM, the actuation frequencies are between 277.100 and 277.300 kHz for the second eigenmode. The variation of actuation frequencies is due to the modified Q_2 and its resulting altered $\omega_{r,2}$. The column presenting the sixth harmonic is without actuation of the second eigenmode. In this case, the external lock-in amplifier is set to demodulate the response at six times the first eigenmode's actuation frequency. This, e.g., results in 280.194 kHz at a $Q_1 = 42$. The

first row of figure 11 is obtained with the natural $Q_1 = 248$ and $Q_2 = 318$, whereas all others are with a $Q_1 = 42$ and different Q_2's. As indicated earlier, the effect of the lower Q_1 is apparent by comparing images obtained with $Q_1 = 248$ and $Q_1 = 42$, but with a $Q_2 = 318$ in both cases (figures 11 (a)–(c) and (g)–(i), respectively). At similar set-points, the increased tip-sample forces of the first eigenmode tapping the surface result in amplified second eigenmode/sixth harmonic signals. Then, the modified Q_2's and constant $Q_1 = 42$ result in differently pronounced features captured from the sample surface. This example shows that the presented compensator enhances the contrast in both imaging methods. Hence, the user would be able to adapt it to the one he might be already using.

In bimodal actuation, in particular ϕ_2 has pronounced sub-features on the soft LDPE half-spheres. These are less pronounced in the A_2 images of the same figure, and not visible in the topography and ϕ_1 images of the first eigenmode (figure 10). This strong effect on A_2 and ϕ_2 can be attributed to the increased second eigenmode's sensitivity to dissipative forces of the sample's materials. Hence, the images form a dissipation map of the different polymers.

The response of the sixth harmonic also captures an increased level of details (figure 11). Dark areas indicate an increased contact time (lower stiffness) resulting in lower
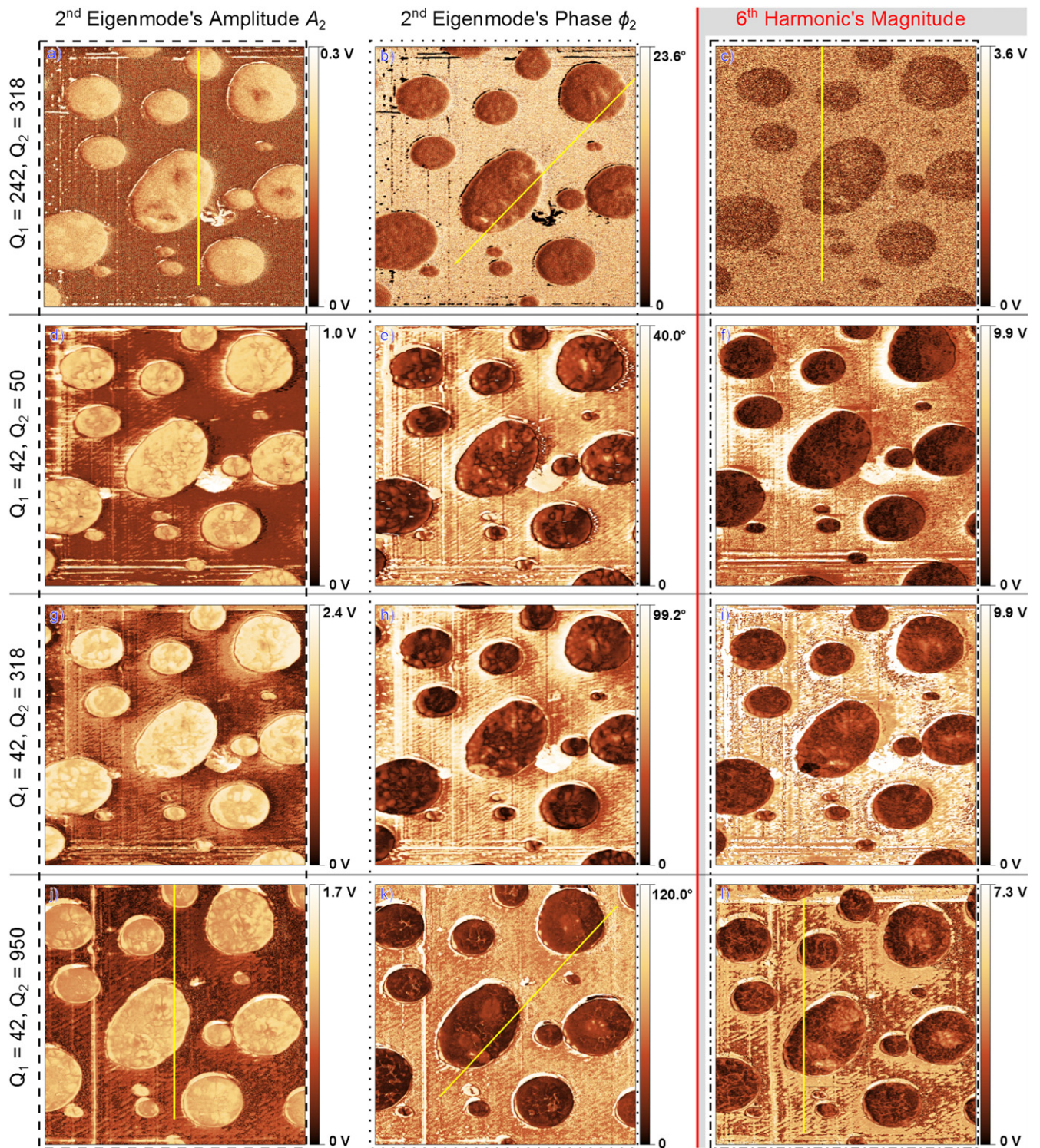
Figure 11. Images presenting A_2 (dashed frame) and ϕ_2 (in degrees, dotted frame) of the second actuated eigenmode as well as the sixth harmonic's signal (dashed–dotted frame). Combinations of Q_1 and Q_2 are indicated for each row of the images.

harmonic amplitudes, as it is the case for the softer LDPE. Lower Q factors in the higher eigenmodes lead to increased harmonic excitations that damp out more quickly [22, 43]. Hence, various details are visible at different Q_2's. These are not visible in the images of the topography and ϕ_1 of the first eigenmode (figure 10). In particular the sixth harmonic's image obtained with $Q_1 = 42$ and $Q_2 = 950$ (figure 11(l)) has

very pronounced contrasts, compared to the images obtained using lower Q_2 factors.

The cross sections highlighted in figures 10 and 11 are compared in figure 12, with two cross sections per signal type. The ordinate's label and legend of each sub-diagram refers to the response captured at specific Q factors. The phase of the first resonance, ϕ_1, does not indicate any difference by
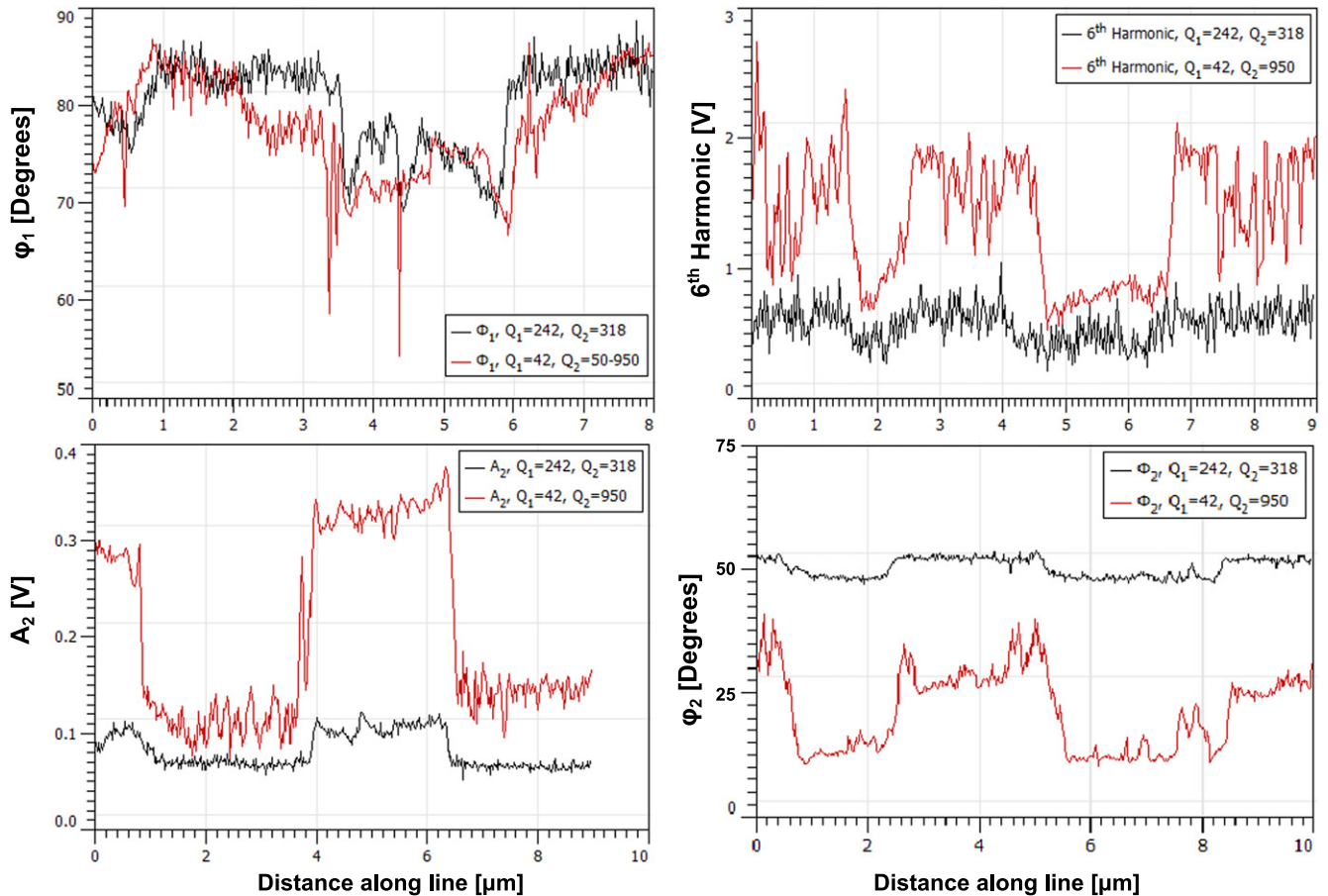
Figure 12. Cross sections comparing various images of figures 10 and 11 at locations indicated by yellow lines. The ordinate's label and legend of each sub-diagram refers to the respective response captured.

decreasing the first eigenmode's Q factor Q_1. In contrast, all signals of the higher eigenmode/harmonic show up to five times higher steps at the material interfaces with overall improved SNRs. The presented methodology is able to detect the different materials both without and with attached compensator. This is due to the large difference in polymer stiffnesses of the used sample. As a conclusion, the compensator's improved contrast allows for the measurement of much smaller material differences that would otherwise be indistinguishable from noise.

Figure 13 is an image that consists of various harmonics captured at different demodulation frequencies with $Q_1 = 42$ and $Q_2 = 950$. Scan speed, size and set-point are similar to those in figure 10/ 11. As indicated, and for approximately 50 lines each, the 512 lines image presents the second to the 11th harmonic responses. As expected, the sixth one is most pronounced.

Beside the enhanced material contrast, the combination of a low Q_1 and high Q_2 has an additional advantage. As the first eigenmode is used for the topography feedback mapping, a low Q_1 has an increased imaging bandwidth. This results in faster tracking speed and thus image acquisition. Figure 14 is a scan of a calibration sample (Anfatec UMG03/PtS) that has 2 μm wide and 58 nm high parallel SiO$_2$ lines on a silicon
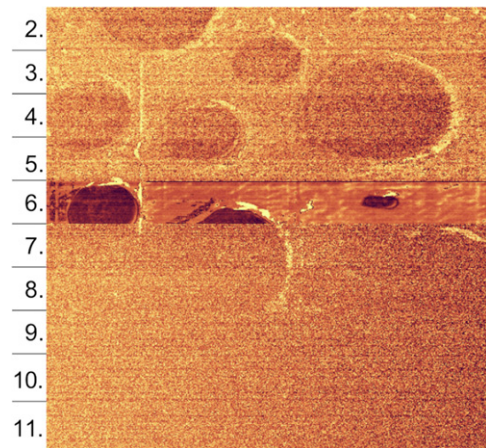

Figure 13. Capture of the different harmonics in a sweep fashion created with $Q_1 = 42$ and $Q_2 = 950$. For 50 lines each, the image of a total of 512 lines presents the harmonics starting at the second one to the 11th one.

substrate with a pitch of 4 μm. The scan rate is 15 line/s and the different Q_1's are indicated. The tracking issue at the higher Q_1 is visible and the lower Q_1 is clearly superior in following the steps.
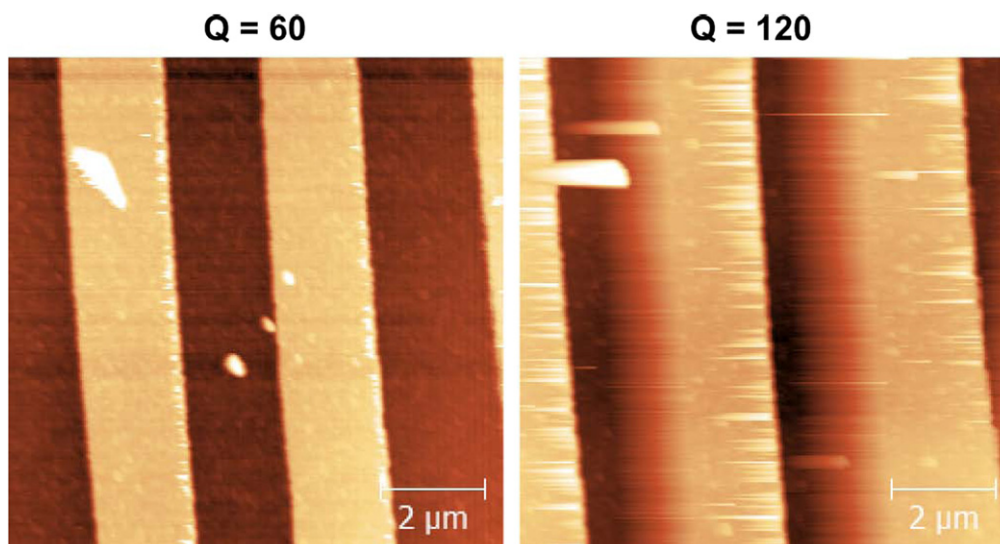
Figure 14. Images of the calibration sample at a scan rate of 15 lines s^{-1} and Q_1 as indicated.

6. Conclusion

We have demonstrated enhanced material contrast and increased imaging rates accomplished by small modifications of a conventional AFM setup. The improvements are achieved by a digital multi-eigenmode compensator that is attached to the AFM. Demonstrated for the first time, the compensator individually modifies each cantilever eigenmode's dynamics and provides imaging capabilities in a multifrequency approach. The proposed methodology allows a flexible way to satisfy the different requirements of the involved eigenmodes, such as fast topography imaging in the first eigenmode and sensitive nanomechanical property mapping in the higher frequencies. Toward material contrast mapping, the best result is achieved with a low Q factor $Q_1 = 42$ for the first and a high Q factor $Q_2 = 950$ for the second eigenmode. With the help of the compensator sample features become visible that are not detected without the modification of the cantilever's dynamics. Further, the compensator can help to distinguish sample stiffnesses that could be indistinguishable from noise otherwise. The low Q_1 also offers the potential for high speed imaging. As demonstrated, the cantilever with a $Q_1 = 60$ is able follow a calibration structure more accurate at $300 \, \mu \text{m s}^{-1}$ tip velocity than with a $Q_1 = 120$. This is in particular beneficial in vacuum environments, where high Q factors prohibit fast scanning. Future extensions of this work could, for example, use the multi-eigenmode compensator to influence the transition between stable oscillation states [44] by using different Q factors.

Acknowledgments

References

[1] Binnig G, Quate C F and Gerber C 1986 Atomic force microscope *Phys. Rev. Lett.* **56** 930–3

[2] Giessibl F J 2003 Advances in atomic force microscopy *Rev. Mod. Phys.* **75** 949–83

[3] Rifai O M E and Youcef-Toumi K 2004 Trade-offs and performance limitations in mechatronic systems: a case study *Annu. Rev. Control* **28** 181–92

[4] Ando T, Uchihashi T, Kodera N, Yamamoto D, Miyagi A, Taniguchi M and Yamashita H 2008 High-speed afm and nano-visualization of biomolecular processes *Pflugers Arch. Eur. J. Physiol.* **456** 211–25

[5] Fleming A J, Kenton B J and Leang K K 2010 Bridging the gap between conventional and video-speed scanning probe microscopes *Ultramicroscopy* **110** 1205–14

[6] Ando T, Uchihashi T, Kodera N, Miyagi A, Nakakita R, Yamashita H and Sakashita M 2006 High-speed atomic force microscopy for studying the dynamic behavior of protein molecules at work *Japan. J. Appl. Phys.* **45** 1897–903

[7] Sulchek T, Hsieh R, Adams J D, Yaralioglu G G, Minne S C, Quate C F, Cleveland J P, Atalar A and Adderton D M 2000 High-speed tapping mode imaging with active q control for atomic force microscopy *Appl. Phys. Lett.* **76** 1473

[8] Cleveland J P, Anczykowski B, Schmid a E and Elings V B 1998 Energy dissipation in tapping-mode atomic force microscopy *Appl. Phys. Lett.* **72** 2613

[9] Garcia R, Gomez C, Martinez N, Patil S, Dietz C and Magerle R 2006 Identification of nanoscale dissipation processes by dynamic atomic force microscopy *Phys. Rev. Lett.* **97** 1–4

[10] Melcher J, Carrasco C, Xu X, Carrascosa J L, Gómez-Herrero J, de Pablo P J and Raman A 2009 Origins of phase contrast in the atomic force microscope in liquids *Proc. Natl Acad. Sci. USA* **106** 13655–60

[11] Stark R W, Drobek T and Heckl W M 1999 Tapping-mode atomic force microscopy and phase-imaging in higher eigenmodes *Appl. Phys. Lett.* **74** 3296

[12] Ulcinas A and Snitka V 2001 Intermittent contact afm using the higher modes of weak cantilever *Ultramicroscopy* **86** 217–22

[13] Woszczyna M, Zawierucha P, Pałetko P, Zielony M, Gotszalk T, Sarov Y, Ivanov T, Frank A, Zöllner J-P and Rangelow I W 2010 Micromachined scanning proximal probes with integrated piezoresistive readout and bimetal actuator for high eigenmode operation *J. Vac. Sci. Technol.* B **28** C6N12

[14] Rodriguez T R and Garcia R 2003 Theory of q control in atomic force microscopy *Appl. Phys. Lett.* **82** 4821

[15] Gunev I, Varol A, Karaman S and Basdogan C 2007 Adaptive q control for tapping-mode nanoscanning using a piezoactuated bimorph probe *Rev. Sci. Instrum.* **78** 043707

[16] Ebeling D, Hölscher H, Fuchs H, Anczykowski B and Schwarz U D 2006 Imaging of biomaterials in liquids: a comparison between conventional and q-controlled amplitude modulation ('tapping mode') atomic force microscopy *Nanotechnology* **17** S221–6

[17] Orun B, Necipoglu S, Basdogan C and Guvenc L 2009 State feedback control for adjusting the dynamic behavior of a piezoactuated bimorph atomic force microscopy probe *Rev. Sci. Instrum.* **80** 063701

[18] Ashby P D 2007 Gentle imaging of soft materials in solution with amplitude modulation atomic force microscopy: Q control and thermal noise *Appl. Phys. Lett.* **91** 254102

[19] Viani M B, Schaeffer T E, Chand A, Rief M, Gaub H E and Hansma P K 1999 Small cantilevers for force spectroscopy of single molecules *J. Appl. Phys.* **86** 2258

[20] Michels T, Guliyev E, Klukowski M and Rangelow I W 2012 Micromachined self-actuated piezoresistive cantilever for high speed spm *Microelectron. Eng.* **97** 265–8

[21] Garcia R and Herruzo E T 2012 The emergence of multifrequency force microscopy *Nat. Nanotechnology* **7** 217–26

[22] Xu X, Melcher J, Basak S, Reifenberger R and Raman A 2009 Compositional contrast of biological materials in liquids using the momentary excitation of higher eigenmodes in dynamic atomic force microscopy *Phys. Rev. Lett.* **102** 060801

[23] Raman A, Trigueros S, Cartagena A, Stevenson A P Z, Susilo M, Nauman E and Antoranz Contera S 2011 Mapping nanomechanical properties of live cells using multi-harmonic atomic force microscopy *Nat. Nanotechnology* **6** 809–14

[24] Stark M, Stark R W, Heckl W M and Guckenberger R 2002 Inverting dynamic force microscopy: From signals to time-resolved interaction forces *Proc. Natl Acad. Sci. USA* **99** 8473

[25] Turner J A and Wiehn J S 2001 Sensitivity of flexural and torsional vibration modes of atomic force microscope cantilevers to surface stiffness variations *Nanotechnology* **12** 322

[26] Guckenberger R 2000 Spectroscopy of the anharmonic cantilever oscillations in tapping-mode atomic-force microscopy *Appl. Phys. Lett.* **77** 3293–5

[27] Sahin O, Quate C F, Solgaard O and Giessibl F J 2010 Higher harmonics and time-varying forces in dynamic force microscopy *Springer Handbook of Nanotechnology* ed B Bhushan (Berlin: Springer) pp 711–29

[28] Stark R W 2004 Spectroscopy of higher harmonics in dynamic atomic force microscopy *Nanotechnology* **15** 347–51

[29] Martinez N F, Lozano J R, Herruzo E T, Garcia F, Richter C, Sulzbach T and Garcia R 2008 Bimodal atomic force microscopy imaging of isolated antibodies in air and liquids *Nanotechnology* **19** 384011

[30] Solares S D and Chawla G 2010 Frequency response of higher cantilever eigenmodes in bimodal and trimodal tapping mode atomic force microscopy *Meas. Sci. Technol.* **21** 125502

[31] Ebeling D and Solares S D 2013 Amplitude modulation dynamic force microscopy imaging in liquids with atomic resolution: comparison of phase contrasts in single and dual mode operation *Nanotechnology* **24** 135702

[32] Chawla G and Solares S D 2009 Single-cantilever dual-frequency-modulation atomic force microscopy *Meas. Sci. Technol.* **20** 015501

[33] Proksch R 2006 Multifrequency, repulsive-mode amplitude-modulated atomic force microscopy *Appl. Phys. Lett.* **89** 113121

[34] Martinez N F, Patil S, Lozano J R and Garcia R 2006 Enhanced compositional sensitivity in atomic force microscopy by the excitation of the first two flexural modes *Appl. Phys. Lett.* **89** 153115

[35] Karvinen K S and Moheimani S O R 2014 Control of the higher eigenmodes of a microcantilever: applications in atomic force microscopy *Ultramicroscopy* **137** 66–71

[36] Ruppert M G, Fairbairn M W and Moheimani S O R 2013 Multi-mode resonant control of a microcantilever for atomic force microscopy *IEEE/ASME Int. Conf. on Advanced Intelligent Mechatronics (AIM)* pp 77–82

[37] Stark R W, Schitter G, Stark M, Guckenberger R and Stemmer A 2004 State-space model of freely vibrating and surface-coupled cantilever dynamics in atomic force microscopy *Phys. Rev.* B **69** 85412

[38] Sahoo D R, de Murti T and Salapaka V 2005 Observer based imaging methods for atomic force microscopy *44th IEEE Conf. on Decision and Control (12–15 December 2005)* pp 1185–90

[39] Ljung L 2010 Perspectives on system identification *Annu. Rev. Control* **34** 1–12

[40] Franklin G F, Powell J D and Workman M L 1998 *Digital Control of Dynamic Systems* 3rd edn (Menlo Park, CA: Addison-Wesley)

[41] Pedrak R, Ivanov T, Ivanova K, Gotszalk T, Abedinov N, Rangelow I W, Edinger K, Tomerov E, Schenkel T and Hudek P 2003 Micromachined atomic force microscopy sensor with integrated piezoresistive sensor and thermal bimorph actuator for high-speed tapping-mode atomic force microscopy phase-imaging in higher eigenmodes *J. Vac. Sci. Technol.* B **21** 3102

[42] Ivanov T, Gotszalk T, Sulzbach T and Rangelow I W 2003 Quantum size aspects of the piezoresistive effect in ultra thin piezoresistors *Ultramicroscopy* **97** 377–84

[43] Rodriguez T R and Garcia R 2002 Tip motion in amplitude modulation (tapping-mode) atomic-force microscopy: Comparison between continuous and point-mass models *Appl. Phys. Lett.* **80** 1646

[44] Kiracofe D, Raman A and Yablon D 2013 Multiple regimes of operation in bimodal afm: understanding the energy of cantilever eigenmodes *Beilstein J. Nanotechnol.* **4** 385–93